Acta Astronautica 215 (2024) 362–372

Contents lists available at ScienceDirect

Acta Astronautica

journal homepage: www.elsevier.com/locate/actaastro

Research paper

Fully kinetic study of facility pressure effects on RF-source magnetic nozzles

Raoul Andriulli [a,*], Shaun Andrews [a], Nabil Souhair [c], Mirko Magarotto [b], Fabrizio Ponti [a]

[a] Alma Propulsion Laboratory, Department of Industrial Engineering, University of Bologna, via Fontanelle 40, Forli, 47121, Italy
[b] Department of Information Engineering (DEI), University of Padova, via Gradenigo 6/b, Padova, 35131, Italy
[c] LERMA Laboratory, Aerospace and Automotive Engineering School, International University of Rabat, Sala al Jadida, Rabat, 11100, Morocco

ARTICLE INFO

Keywords:
Particle-in-cell
Cathode-less RF plasma thruster
Facility pressure
Magnetic nozzle
Xenon

ABSTRACT

A fully kinetic 2D axisymmetric Particle-in-Cell (PIC) model is used to examine the effects of background facility pressure on the plasma transport and propulsive efficiency of magnetic nozzles. Simulations are performed for a low-power (150 W class) cathode-less radio-frequency (RF) plasma thruster, operating with xenon, between background pressures up to 10^{-2} Pa and average electron discharge temperatures of 4–16 eV. When the electron temperature within the near-plume region reaches 8 eV, a decisive reduction in performance occurs: at 10^{-2} Pa, in-plume power losses surpass 25% of the discharge energy flux. Given that the ionisation energy for Xe is 12 eV, the 8 eV threshold indicates that a consistent percentage of electrons has energy enough to trigger ionisation. On the other hand, when the temperature is below such threshold, the primary collisions are charge-exchange and inelastic ion scattering, and the power loss remains less than 10%. It is established that losses in the considered thruster are significant if the facility pressure is greater than 10^{-3} Pa, at absorbed powers larger than 130 W. At the nominal 150 W, this results in a 15% thrust reduction. When facility pressure is taken into consideration over ideal vacuum simulations, numerical error is reduced to <30% when compared to experimental thrust measurements at 10^{-3} Pa.

1. Introduction

In recent years, the increasing demand for simple and low-cost electric propulsion (EP) for small satellites has given rise to a growing interest in low-power (<250 W) cathode-less magnetically-enhanced plasma thrusters (MEPT) [1]. This category primarily includes the Helicon Plasma Thruster (HPT) [2] and the Electron Cyclotron Resonance Thruster (ECRT) [3]. In such systems, the plasma acceleration is driven by a magnetic nozzle (MN): a divergent magneto-static field generated by a set of solenoids or permanent magnets. The MN radially confines the hot quasi-neutral partially-magnetised plasma beam and accelerates it via the conversion of thermal energy into directed axial kinetic energy, therefore enhancing thrust [4].

MEPTs can operate on a wider range of propellants (e.g iodine and water) [5]; these are often less expensive than traditional xenon, because of their greater abundance, and are easier to store due to the non-requirement of pressurised tanks [6,7]. From a systems perspective, MEPTs can also be less-complex than state-of-the-art devices (e.g. gridded ion and Hall effect thrusters (HET)) as they do not require a separate dedicated neutralising electron source (e.g. a hollow cathode), which increases the power and propellant consumed, and is a known failure mechanism [8]. Due to the absence of plasma-immersed electrodes, MEPTs are highly resistant to erosion, which is often the lifetime-limiting aspect of conventional electric propulsion systems [9]. MNs also have no physical walls, thus avoiding thermal loading and further erosion issues.

However, since the ion acceleration occurs external to the plasma source — in a region that can be several times the thruster radius — devices that use a MN are highly susceptible to so-called facility effects [10,11]. EP thrusters interacting with the facility environment is a widely recognised problem in the field and calls into question the ability to extrapolate measured performance of such systems to their intended environment in space [12,13].

While facility effects continue to be an on-going area of research for most forms of EP, MEPTs pose a particular challenge: experimental efforts have revealed that their response to facility effects, particularly the presence of excess neutrals due to finite pumping speed, is different from other state-of-the-art EP technologies [14]. The experiments of Vialis et al. [15], with an ECRT operating on xenon at 40 W, revealed that the high-vacuum thrust efficiency of 12.5% at 6×10^{-4} Pa would drop to 9% at 7.2×10^{-4} Pa, and 3.9% at 1.3×10^{-3} Pa facility pressure. It was found that the divergence of plasma within the plume increased, on-axis ion current density decreased by almost 60%, and the thruster floating potential decreased by a factor of approximately 0.25 as background pressure was raised. Studies of a 100 W HPT, that

* Corresponding author.
E-mail address: raoul.andriulli@unibo.it (R. Andriulli).

https://doi.org/10.1016/j.actaastro.2023.12.014
Received 7 June 2023; Received in revised form 29 October 2023; Accepted 8 December 2023
Available online 13 December 2023

were conducted at higher facility pressures of $1.9 \times 10^{-3} - 8.8 \times 10^{-3}$ Pa, revealed similar trends [16].

In both cases, the changes in efficiency and divergence were counter to what is found for more established forms of EP such as HETs [17–21]. These latter technologies typically improve in performance with increasing pressure. Kerber et al. [18] describes how the beam, current, and mass utilisation efficiencies of a HET are affected by the background pressure. The study found that decreasing background pressure resulted in a decrease in mass and current efficiencies (the latter defined as the ratio of beam to discharge currents) of the tested HET, while the beam efficiency (related to the divergence angle) was only slightly affected. Snyder [21] discusses the dependence of absolute HET thrust on pressure and power. The study found that the highest power had the largest dependence on pressure, with little-to-no measurable dependence at the lowest power. However, the relative change of thrust with pressure was consistent for all powers above 1 kW, with about 2–4% higher thrust at 1.3×10^{-3} Pa compared to the lowest facility pressure at each power level ($\sim 4 \times 10^{-4}$ Pa). The arguments that have been employed for these systems to explain facility effects thus do not seem to apply to devices utilising a MN.

Several theories have previously been put forward to explain the performance detriment of MNs due to non-negligible facility pressure. These have included background neutral ingestion impacting the power balance and consequent plasma production in the source region [16], as well as energy losses due to the onset of secondary discharges occurring outside the thruster plume when the neutral environment is sufficiently high [15]. Vialis [15] and Collard and Jorns [22] have shown that the presence of excess neutrals can also directly impact the dynamics of the MN itself, i.e. the ability to convert thermal energy into directed kinetic energy. Experiments demonstrated, for example, that the acceleration profile of ions is reduced at high facility pressure. This was numerically confirmed by Andrews et al. [23], who suggested that ion drag from charge and momentum exchange collisions in the plume substantially delays the ambipolar ion acceleration.

Wachs et al. [24] found that the performance loss can largely be attributed to electron–neutral inelastic collisions within the plume that significantly reduce the amount of power available to accelerate ions. The same experimental campaign showed that potential drop decreased by 20% as background pressure increased from 9×10^{-5} Pa to 7×10^{-3} Pa. From additional tests conducted in Ref. [25], with a background pressure varying between 1.3×10^{-4} Pa and 3.4×10^{-3} Pa, Wachs calculated that, at maximum pressure, almost 40% of the power entering the plume was consumed mainly by inelastic collisions. This correlates with the results of previous numerical work [23,26], where it was clear that power entering the plume, in the form of both ion inertia and electron pressure, is consumed by ionisation and excitation collisions with the neutral gas plume of the thruster. Physically, these collisions remove the critical thermal energy introduced to the electrons in the source region before it can be successfully converted to ion kinetic energy. This however, only applies to high-T_e (i.e. >10 eV) plasma sources where inelastic collisions dominate, neglecting other hypothesised effects such as increased plasma friction, cross-field transport and early detachment from the MN.

It is therefore critical that numerical models must be augmented to accurately describe plume dynamics in thrusters operating in finite background pressure conditions. The aim of this study is to conduct a thorough investigation of the performance loss mechanisms induced by non-negligible facility pressures across a wide range of thruster operating powers. To this end, a recently developed numerical suite [26,27], which consists of a 0D Global Source Model (GSM) of the plasma source, coupled to a fully kinetic Particle-in-Cell (PIC) model of the MN, is used to investigate in detail facility pressure effects on the MN performance of a 150 W class MEPT. Section 2 describes the GSM and PIC models, and the numerical setup. In Section 3, the thrust and power balances in the MN region are presented to enable characterisation of the loss mechanisms. Section 4 is dedicated to the presentation and discussion of results, while Section 5 gives the conclusions.

2. Thruster physical and numerical model

2.1. Global source model

The MEPT considered in this work is a cathode-less RF plasma thruster. A 0D Global Source Model (GSM), as presented in Refs. [26,28], was used to evaluate the plasma properties at the exit section of the source tube. This volume-averaged model is based on the following main assumptions: (i) cylindrical geometry of the plasma source; (ii) axisymmetric magnetostatic field; and (iii) the magnetic cusps in the source are taken into account by means of semi-empirical corrections. The governing equations that describe the plasma dynamics are the species density flux and electron power balance,

$$\frac{dn_I}{dt} = R^I_{chem} - R^I_{wall} - R^I_{*} + R^I_{in}, \tag{1}$$

$$\frac{d}{dt}\left(\frac{3}{2} n_e \langle T_e \rangle\right) = P'''_a - P'''_{chem} - P'''_{wall} - P'''_{*}, \tag{2}$$

where n_I is the number density of species I (the subscript e refers to electrons). Among these, ions, ground-state neutrals and excited states are present. The excited states of Xe are included in a lumped form [28]. Hereafter, the electronic states $5p^5 6s^1$ and $5p^5 6p^1$ will be referred to as 1S and 2P, respectively, according to Paschen's notation [29].

R_{chem}, R_{wall}, R_{*}, R_{in} are the particle density fluxes related to chemical reactions, wall losses, particle outflow and particle inflow respectively. Similarly, P'''_a, P'''_{chem}, P'''_{wall} and P'''_{*} are the power densities of the RF power absorbed into the plasma, the power exchanged/lost via chemical reactions, the energy flux losses at the walls, and the power associated to the particle outflow respectively. $\langle T_e \rangle$ is the global-averaged electron temperature. Non-uniformity in the plasma profiles within the source are taken into account by means of semi-empirical coefficients h_L and h_R, explained in Refs. [30,31]. A more detailed description of the model can be found in the Appendix.

Given the absorbed power density P'''_a, propellant mass flow rate $\dot{m}$, and magnetic field $\mathbf{B}$, the GSM solves the system of equations to provide to the PIC model the ion and electron mass flow rate and the electron temperature, namely $\dot{m}_{i*}$, $\dot{m}_{g*}$ and T_{e*}; the subscript $*$ denotes the reference source properties at the exit for the PIC model.

2.2. Particle-in-Cell

The plasma topology in the MN has been simulated with an in-house adaption of the fully kinetic axisymmetric 2D3V PIC code *Starfish* [23,32], which has been experimentally validated in Refs. [23,27,33]. The simulation domain is shown in Fig. 1; it consists of a cylindrical 2D space (z, r). The aim of this work is to simulate purely the plume expansion, hence the source is not included in the domain. As mentioned above, the plasma injection parameters are provided by the GSM. The flow is injected at the source tube outlet (I). The external boundaries (III) are treated as open to vacuum, connected to the outlet (I) via a virtual free-space capacitance which ensures equal ion and electron current streams to the infinity at steady-state. Boundary (II) is the axis of symmetry. The subscripts $*$, 0, b and ∞ shall refer to properties within the plasma source (reference), at the thruster outlet boundary (I), at the open boundaries (III) and at the virtual infinity respectively. The subscript B shall refer to the integral sum of local properties along the open boundaries. Likewise, the superscripts + and − shall refer to the forward and backward-marching components of the plasma properties.

Electrons e, ions i and neutrals g, are all tracked as macro-particles and their motion is propagated with the standard leap-frog Boris algorithm:

$$\frac{\mathbf{v}^{n+1/2} - \mathbf{v}^{n-1/2}}{\Delta t} = \frac{q_I}{m_I}\left(\mathbf{E}^n + \frac{\mathbf{v}^{n+1/2} + \mathbf{v}^{n-1/2}}{2} \times \mathbf{B}\right), \tag{3}$$

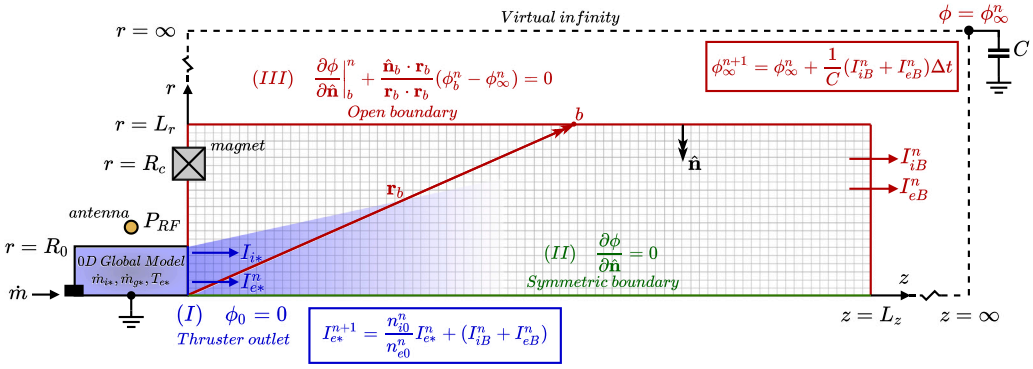

Fig. 1. Simulation domain and boundary conditions: (I) is the source tube outlet; (II) is the symmetric boundary; (III) is the open boundary.

$$\frac{\mathbf{r}^{n+1} - \mathbf{r}}{\Delta t} = \mathbf{v}^{n+1/2}, \tag{4}$$

where $\mathbf{r}^n$ is the particle position at time-step n with velocity $\mathbf{v}^n$, Δt is the time-step, $\mathbf{E}$ is the electric field, and $\mathbf{B}$ is the static magnetic field. The currents induced in the plume are negligible [34], hence the magnetic fields can be assumed to be constant. As a result, the electric field $\mathbf{E}$ is curl-free and its potential field ϕ can be solved according to the Poisson's equation,

$$\varepsilon_0 \nabla^2 \phi = -\rho, \tag{5}$$

where $\rho = e(n_i - n_e)$ is the local charge density and ε_0 is the vacuum permittivity. At each time-step, the new electric field $\mathbf{E}$ is updated by evaluating

$$\mathbf{E} = -\nabla\phi. \tag{6}$$

2.2.1. Boundary conditions

A reference potential $\phi = 0$ is assigned to the source tube outlet (I), the $r = 0$ axis (II) is symmetric, hence, the zero-Neumann boundary condition $\partial\phi/\partial\hat{\mathbf{n}} = \mathbf{0}$ is applied there, with $\hat{\mathbf{n}}$ the unit vector normal to the surface. The remaining open boundaries (III) are closed by a non-stationary Robin condition introduced by Andrews et al. [23],

$$\left.\frac{\partial\phi}{\partial\hat{\mathbf{n}}}\right|^n_b + \frac{\hat{\mathbf{n}}_b \cdot \mathbf{r}_b}{\mathbf{r}_b \cdot \mathbf{r}_b}\left(\phi^n_b - \phi^n_\infty\right) = 0, \tag{7}$$

where $\mathbf{r}_b$ is the vector distance from the centre of the source outlet (I) to the location on the open boundary (III) and ϕ_∞ denotes the free-space plasma potential at infinity.

At each time-step, particles are injected from the source outlet boundary (I). Since the 0D GSM has been used to estimate the plasma properties, a uniform density is imposed. Regarding the velocity, for all species, a Maxwellian distribution is assumed [35],

$$f^+_I(\mathbf{v}_I) = \sqrt{\frac{m_I}{2\pi k_B T_{I*}}} \exp\left(-\frac{m_I}{2k_B T_{I*}}|\mathbf{v}_I - \mathbf{u}_I|^2\right) H(v_{Iz}), \tag{8}$$

where T_{I*} is the reference species temperature and k_B is the Boltzmann constant. The drift velocity $\mathbf{u}_I$, imposed along the z direction, is equal to the Bohm speed for both ions and electrons $\mathbf{u}_{i,e} = \langle c_*, 0, 0\rangle$, where $c_* = \sqrt{k_B T_{e*}/m_i}$. Neutrals possess free-molecular thermal velocity $\mathbf{u}_g = \langle \bar{v}_g/4, 0, 0\rangle$, where $\bar{v}_g = \sqrt{8k_B T_{g*}/\pi m_g}$. $H()$ is the Heaviside function, since only forward-marching distributions ($v_{Iz} > 0$) can be imposed.

Ions and electrons (and neutrals) returning to the source are absorbed; ions and neutrals reaching the open boundaries are also absorbed. For electrons at the open boundaries, an energy-based reflection criterion is used to account for the trapped population returned by the ambipolar potential drop [23]. The kinetic energy of electrons KE_e is compared to the trapping potential PE_b on the boundary node:

$$KE_e = \frac{1}{2} m_e |\mathbf{v}_e|^2; \tag{9}$$

$$PE_b = e(\phi_b - \phi_\infty). \tag{10}$$

If $KE_e < PE_b$ the electron is trapped, so it is reflected back with velocity $-\mathbf{v}_e$. Else, it is a free electron to be removed from the domain.

From this energy-based criterion, there is a value of ϕ_∞ that reflects sufficient electrons to maintain a current-free plume. Therefore, the value of ϕ_∞ is self-consistently controlled via a virtual free-space capacitance C,

$$\phi^{n+1}_\infty = \phi^n_\infty + \frac{1}{C}(I^n_{iB} + I^n_{eB})\Delta t, \tag{11}$$

where I_{iB} and I_{eB} are the global sum ion and electron currents leaving the open boundaries (III). This method inherently guarantees that, once at steady-state, the ion and electron currents streaming to infinity are equal.

During the transient, any non-zero net current leaving the open boundaries (III) must be re-injected into the domain via the thruster outlet (I) to complete the circuit. In addition, the injected electron current I_{e*} is controlled in order to enforce the quasi-neutrality condition at the source outlet (I). From these considerations, the following conditions are imposed to particles injected at boundary (I). Ions are injected with a constant current given by $I_{i*} = en_{i*}c_*A_0$, where A_0 is the area of the source outlet. The injected electron current is updated each time step according to

$$I^{n+1}_{e*} = (I^n_{iB} + I^n_{eB}) + \frac{n^n_{i0}}{n^n_{e0}} I^n_{e*}, \tag{12}$$

where the first term completes the circuit and the second enforces the quasi-neutrality. Considering that injected electrons are Maxwellian, the initial value of the current is set to be $I^0_{e*} = -en_*(\bar{v}_{e*}/4 + c_*)A_0$. The neutral flux is imposed as $\Gamma_{g*} = n_{g*}\bar{v}_g/4A_0$. Since ions are only accelerated outward by the electric field, and neutrals diffuse guided by the outer pressure gradient, no treatment is required for a possible backflow of heavy particles.

For a more detailed description of this PIC formulation, including validation, derivation of the Robin condition, domain-independence studies, and a numerical sensitivity analysis, the reader is directed to the previous work of Andrews et al. [23,36].

2.2.2. Collisions

The model considers electron–neutral elastic and inelastic (i.e., ionisation and excitation) scattering, ion–neutral scattering, ion–neutral charge exchange (CEX), Coulomb collisions and an equivalent anomalous collisionality. Neutrals are at ground state (i.e. not excited) by default and any excited states are assumed to decay immediately. Collisions between different species are handled with the Monte Carlo Collisions (MCC) method [37], while same species interactions were considered with full Direct Simulation Monte Carlo (DSMC) treatment [38]. The list of collisions implemented in the numerical suite

Table 1
Interactions cross-sections.

Reactions	Reaction-type	
$e + e \longrightarrow e + e$	Coulomb scattering	[41]
$e + Xe^+ \longrightarrow e + Xe^+$	Coulomb scattering	[42]
$e + Xe^+ \longrightarrow e + Xe^+$	Bohm collision	[43]
$e + Xe \longrightarrow 2e + Xe^+$	Ionisation	[42]
$Xe^+ + Xe \longrightarrow Xe^+ + Xe$	Momentum exchange	[42]
$Xe^+ + Xe \longrightarrow Xe + Xe^+$	Charge exchange	[42]
$e + Xe \longrightarrow e + Xe$	Elastic scattering	[42]
$Xe + Xe \longrightarrow Xe + Xe$	Elastic scattering	[42]
$e + Xe \longrightarrow e + Xe_{1S}$	Excitation	[28]
$e + Xe \longrightarrow e + Xe_{2P}$	Excitation	[28]

and their respective references are provided in Table 1. Anomalous collisions are taken into account through the empirical Bohm model [39], with a diffusion coefficient $\alpha_{an} = 1/64$. When considering electron–neutral excitation interactions, taking into account the dynamics of each fine-structure excitation state would represent an unbearable computational effort. Instead, a lumping of the energy levels is performed, implemented according to Souhair et al. [28]. Excited states are lumped to divide resonant and metastable species as well as the previously introduced 1S and 2P. This lumping methodology requires the assumption of local thermodynamic equilibrium (LTE) according to McWhirter [40]. For the temperatures handled in this work ($T_e < 20$ eV), and the maximum energy gap, this gives a threshold value of $n_e > 10^{16}$ m^{-3} [28]. Since more than 95% of the excitation collisions takes place where such density criterion is satisfied, LTE can be considered a reasonable assumption within the scope of this paper.

If a collision takes place, the electron is assumed to lose energy equal to the lumped excitation energy ($\Delta U_{IJ} = U_J - U_I$), i.e. $E_e^{n+1} = E_e^n - \Delta U_{IJ}$, and its speed is reduced accordingly.

The lumped excitation cross-section can be evaluated by means of an adapted version of the procedure defined in [28],

$$\sigma_{ex_{IJ}} = \sum_i^{N_i} \left[\frac{\sum_j^{N_j} \sigma_{ex_{ij}}}{\sum_k^{N_i} \frac{g_k}{g_i} \exp\left(-\frac{U_k - U_i}{k_B T_g}\right)} \right], \tag{13}$$

where $\sigma_{ex_{IJ}}$ represents the cross-section for the lumped state I to J, $U_k - U_i$ is the energy difference between the kth and the ith fine-structure levels, g_k and g_i are the statistical weights, and T_g is the neutral gas temperature.

2.2.3. Numerical acceleration

The simulation time-step should be small enough to resolve plasma frequency $\omega_{pe} = \sqrt{n_e e^2/\varepsilon_0 m_e}$; this, combined with fine mesh requirements where spacing is imposed by the Debye length $\lambda_D = \sqrt{\varepsilon_0 k_B T_e / n_e e^2}$, results in an unmanageable computational load.

In order to reduce this effort, two different numerical acceleration approaches have been adopted [44]. The vacuum permittivity is increased by a factor γ^2; the Debye length then increases by γ, allowing for a less refined mesh and fewer macro-particles. Plasma frequency also slows by a factor $1/\gamma$, hence a larger time-step may be chosen.

Second, the heavy particle mass (i.e. m_i and m_g) is reduced by a factor f; this increases their velocity by $\sqrt{f}$. The combination of these reduces the simulation time by approximately $\gamma^2\sqrt{f}$. Ref. [23] reports a sensitivity analysis on the values of γ and f used in the PIC model. All the results that are shown in this work are presented unscaled.

3. Performance indicators

In order to define the propulsive performance and to analyse the power balance of the MN, maps of macroscopic quantities (e.g., density, velocity, temperature) are computed by integrating the moments of the distribution functions computed with the PIC [45]. In the following, the relations used to derive performance indicators (e.g., thrust) from these distributions are presented.

3.1. Thrust

The total thrust F has been evaluated as the combination of the force produced by the plasma expansion through the source tube outlet F_0 and the force imparted by the MN $F_{j\times B}$,

$$F = F_0 + \underbrace{\iiint_V -j_{e\theta} B_r \, dV}_{F_{j\times B}}, \tag{14}$$

where $j_{e\theta} = -e n_e u_{e_\theta}$ is the azimuthal electron current density (u_{e_θ} being the azimuthal electron speed), B_r is the radial component of the magnetic field $\mathbf{B}$, and V is the PIC domain volume.

The plasma source contribution to thrust F_0 can be obtained by computing Eq. (15) at the exit section of the plasma source $dS = dA_0$ [46].

$$F = \oiint_S \sum_I \left(m_I n_I \mathbf{u}_I \mathbf{u}_I + p_I \bar{\bar{\mathbf{I}}} + \bar{\bar{\pi}}_I \right) \cdot \hat{\mathbf{n}} \, dS, \tag{15}$$

where $p_I = k_B n_I T_I$ is the scalar pressure, $\bar{\bar{\mathbf{I}}}$ is the identity tensor, and $\bar{\bar{\pi}}_I$ is the stress tensor [47].

3.2. Power balance

The energy equation [47], for a steady-state flow reads

$$P_{kin,I} + P_{T,I} + Q_I + P_{coll} = 0. \tag{16}$$

The different terms represent the species kinetic ($P_{kin,I}$) and thermal convection powers ($P_{T,I}$), the heat flux (Q_I) and the overall power losses due to collision between particles I and particles of a different species. The following power contributions have then been considered in order to evaluate the propulsive efficiencies:

$$P_{kin,I} = \oiint_S \frac{1}{2} n_I m_I u_I^2 \mathbf{u}_I \cdot \hat{\mathbf{n}} \, dS; \tag{17}$$

$$P_{T,I} = \oiint_S \frac{5}{2} n_I T_I \mathbf{u}_I \cdot \hat{\mathbf{n}} \, dS. \tag{18}$$

P_* is the source tube exhaust power as provided by Eq. (2) of the GSM; it can also be given by

$$P_* \approx \sum_I P_{kin,I}(dA_0) + \sum_I P_{T,I}(dA_0) + \sum_I Q_k(dA_0). \tag{19}$$

For collisional interactions, Eq. (20) allows the computation of the power involved in the particular elastic or inelastic interaction:

$$P_{coll_{IJ}} = \iiint_V n_I \nu_{IJ} \Delta E_{IJ} \, dV, \tag{20}$$

for interaction between species I and J. ν is the collision frequency and ΔE_{IJ} is the energy variation that depends on the particular reaction.

The central hypothesis of this work posits that variations in MN performance under increasing facility pressure can be elucidated by the irreversible loss of ion and electron energy caused by elastic and inelastic collisions with the background gas per Eq. (16). This does not necessarily mean that the overall power of the expanding plasma decreases. When considering the working principle of the magnetic nozzle, neutral particles cannot contribute to the Lorentz force, thus no contribution to thrust is provided by the cold gas once it has exited the discharge chamber. Therefore, the power that is exchanged towards neutrals (belonging to the plume or the background) will be considered (and referred to) as loss terms, a principle also adopted in Refs. [25,48].

Regarding the charge-exchange interaction between ions and background neutrals, whenever a fast ion collides with a neutral particle, a fast atom and a slow ion will be generated. Given the aforementioned inability of neutral particles to interact with the thruster via the MN, the net momentum gain of the n_g population is not expected to result in a performance increase [48]. Previously, background CEX interactions have been experimentally proven to widely contribute to

Table 2
Plasma parameters at the source tube exit for different absorbed power.

P_a [W]	T_{e*} [eV]	$n_{i*} \times 10^{18}$ [m^{-3}]	$n_{g*} \times 10^{19}$ [m^{-3}]	η_u	η_s
60	4.20	1.22	2.75	0.59	0.059
90	8.32	1.41	0.30	0.95	0.126
130	13.76	1.12	0.15	0.98	0.148
150	16.34	1.03	0.13	0.98	0.153

ion momentum and energy loss in the plume [49], therefore they will be considered losses.

For the generic elastic collision, ΔE_{IJ} coincides with the kinetic energy of the reduced system,

$$\Delta E_{IJ}^{\mathrm{el}} = \frac{1}{2} m_r (|\mathbf{u}_I| - |\mathbf{u}_J|)^2, \tag{21}$$

where m_r is the reduced mass. In the case of inelastic collision losses, the energy loss is instead fixed according to the relevant threshold energy gap (e.g. ionisation and excitation).

The following three main efficiencies can then be defined for the MN:

$$\eta_{conv} = \frac{P_{kin,i}}{P_*}; \tag{22}$$

$$\eta_{div} = \frac{P_{kin,i}^{(z)}}{P_{kin,i}}; \tag{23}$$

$$\eta_{MN} = \frac{\sum_I \left(P_{kin,I}^{(z)} + P_{T,I} \right)}{P_*}. \tag{24}$$

η_{conv} is the internal to ion-kinetic energy conversion efficiency, η_{div} is the ion divergence efficiency (i.e. a measure of ion confinement), and η_{MN} represents the overall MN efficiency [46].

4. Results and discussion

4.1. Thruster specifications

The thruster considered in this work is a laboratory prototype, derived from the REGULUS-150 cathode-less RF MEPT [27]. The plasma source is a cylindrical tube of length $L_s = 0.100$ m and radius $R_s = 0.0085$ m. The on-axis magnetic field intensity at the MN throat is $B_0 \approx 450$ G; the field topology is given in Fig. 3(a). The RF antenna is a 0.02 m long five-turn copper coil, with a wire width of $w_A = 0.002$ m [26]. Xenon propellant is delivered to the injector with mass flow rate $\dot{m} = 0.25$ mg/s. The antenna coupling efficiency is assumed to be $\eta_{RF} \approx 0.7$.

4.2. Operating condition and neutral gas density

The MN has been simulated at a range of absorbed powers, with source reference properties from the GSM given in Table 2. For the main discussion hereafter, the $P_a = 60$ W and $P_a = 130$ W cases are focused upon: the former is a low-temperature ($T_{e*} < \Delta E_{ion} = 12.1$ eV), high neutral density ($n_{g*} > n_{i*}$) mode; the latter is a higher temperature ($T_{e*} > \Delta E_{ion}$), low neutral density ($n_{g*} < n_{i*}$) regime. This pronounced variation in the neutral concentration can be explained by looking at Fig. 2. Defining the mass utilisation efficiency ($\eta_u = \dot{m}_{i*}/\dot{m}$) of the RF-source as the ratio between the ion mass flow rate and the overall flow rate, it is quite evident how below the threshold of 80 W, the efficiency rapidly drops, resulting in a substantial difference in outlet parameters. Fig. 2 also shows the source efficiency $\eta_s = P_*/P_a$ defined as the ratio between the power at the exhaust of the source chamber and the RF power absorbed by the plasma.

Background pressure is included in the PIC by setting a fixed uniform neutral distribution n_g^{back} via the ideal gas law,

$$p_{\mathrm{back}} = n_g^{\mathrm{back}} k_B T_g^{\mathrm{back}}, \tag{25}$$

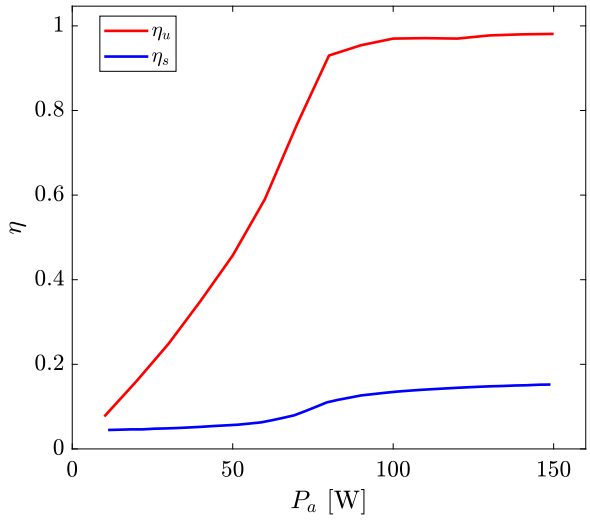

Fig. 2. Mass utilisation efficiency η_u and source efficiency η_s as function of the absorbed power P_a.

at a nominal temperature of $T_g^{\mathrm{back}} = 300$ K. Starting from the vacuum scenario $n_g^{\mathrm{back}} = 0$ m^{-3} at $p_{\mathrm{back}} = 0$ Pa, this leads to $n_g^{\mathrm{back}} = 2.51 \times 10^{18}$ m^{-3} at $p_{\mathrm{back}} = 10^{-2}$ Pa.

Before advancing in the study, a quick consideration about the hypothesis of a uniform background distribution is made. When dealing with vacuum chamber gas distribution, the gradient of the neutral gas pressure is generally dependent on the individual chamber arrangement. Moreover, several experimental measures [50,51] and DSMC [52] simulations have proven the neutral map to be basically constant around the plume expansion region, as long as the vacuum chamber is well dimensioned for the experiment. Therefore, the assumption of a constant background allows for relatively valid results while not losing the generality of the study. Fig. 3(b) shows the normalised neutral density from the thruster plume n_g^{plume}, pre-computed with the DSMC method. The on-axis combination of both plume and background density $n_g^{\mathrm{tot}} = n_g^{\mathrm{plume}} + n_g^{\mathrm{back}}$ is then given in Fig. 3(c) for $P_a = 60$ and 130 W for $p_{\mathrm{back}} = 0 - 10^{-2}$ Pa. Due to the lower n_g^{plume} of the high-power case (from greater mass utilisation efficiency) there is a more decisive variation of the total density with changing facility pressure.

4.3. Plasma profiles

In order to gain insight into the plume topology, the 2D plasma profiles are provided in Fig. 4 for the 130 W case. Fig. 4(a) and (b) show electron number density distribution for vacuum conditions and 10^{-2} Pa respectively. At low-pressure, the plume is highly-collimated and the expansion is confined within the outermost magnetic field line (OMFL) connected to the source. Only a small fraction of electrons is able to escape the confinement of the MN; this is due to their high energy. In Fig. 4(b), a more diffusive behaviour appears as the electrons that manage to escape from the OMFL are now more than just the high energy tail of the discharge Maxwellian distribution.

Despite this enhanced cross-field diffusion, the density does not considerably reduce in the downstream region of the plume. This is because the increased neutral background produces significant in-plume ionisation. Low-energy ions are formed in the near-field and are therefore heavily influenced by the radial electric field; the ions accelerate radially and form a secondary density cloud similar to that seen from CEX. With the possible exception of ions that have experienced CEX collisions, ions born in the near-field plume region also experience a smaller potential drop than ions born in the source tube. The mean

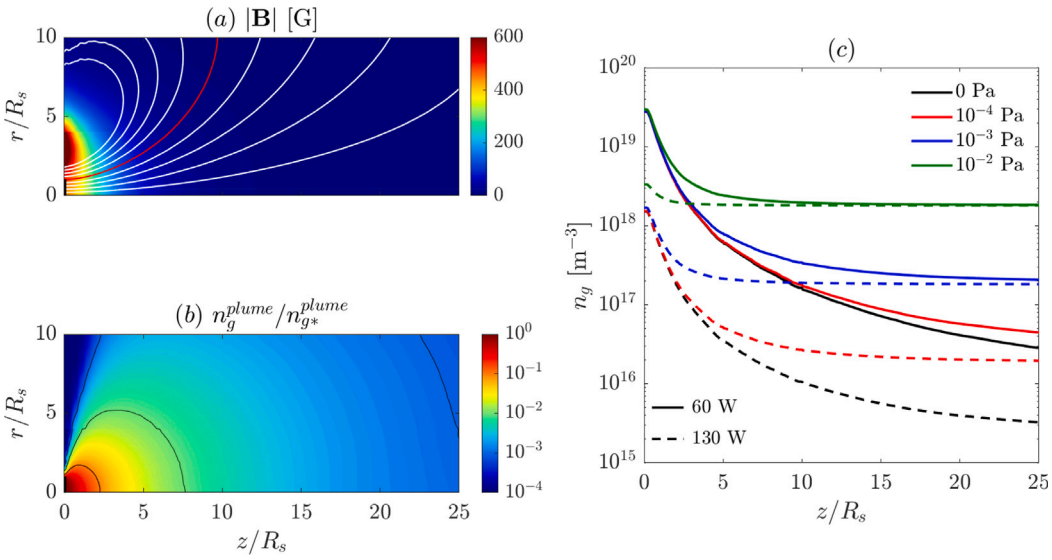

Fig. 3. (a) Magnitude of the magnetic flux density |**B**|. The outermost magnetic field line connected to the source is given by the red contour; (b) Normalised neutral gas density from the plume discharge $n_g^{\text{plume}}/n_{g*}^{\text{plume}}$; (c) On-axis total neutral gas density n_g^{tot} for $P_a = 60$ W and 130 W. (For interpretation of the references to colour in this figure legend, the reader is referred to the web version of this article.)

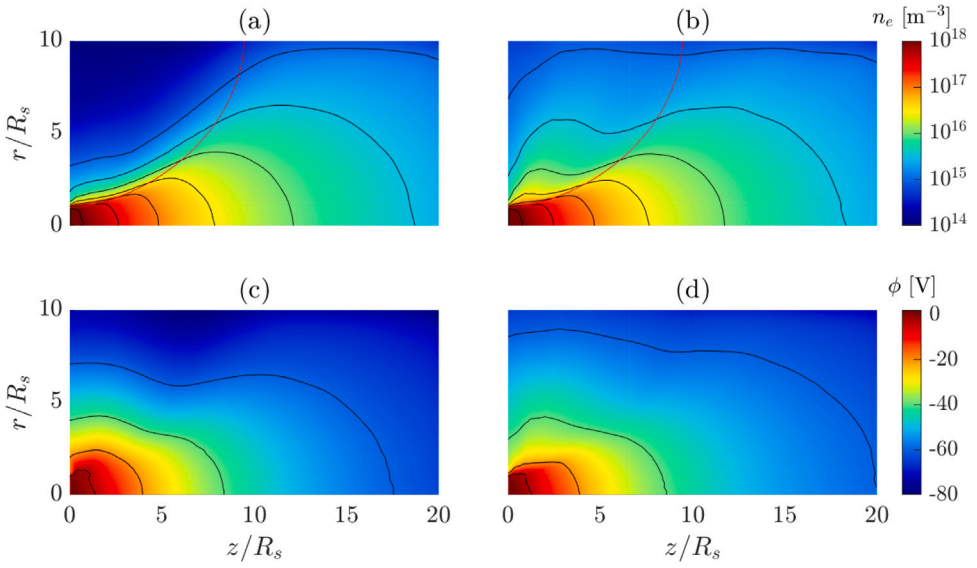

Fig. 4. 2D profiles of (a)(b) electron number density n_e (c)(d) plasma potential ϕ for 130 W for background pressure 0 Pa (left) and 10^{-2} Pa (right) for $P_a = 130$ W. The red line indicates the outermost magnetic field line connected to the plasma source. (For interpretation of the references to colour in this figure legend, the reader is referred to the web version of this article.)

ion speed within the fluid may be significantly decreased by this newly ionised population, serving as an effective drag term on the ions [23].

Fig. 4(c) and (d) give the plasma potential. Note that the enhanced radial potential peak observed in Ref. [23] does not appear in Fig. 4(c) since the near-exit neutral density at 130 W is insufficient to produce the necessary ion–neutral collisions, but a mild ion-confining potential barrier is still present. This structure completely fades at 10^{-2} Pa in Fig. 4(d). In particular, the plasma potential has a smoother monotonic gradient in all directions. The downstream potential drop is then reduced by approximately 5 V by the domain boundaries.

Fig. 5 provides the radial profiles of n_e and ϕ at $z = 5$ mm. Fig. 5(a) shows the radial electron density; it is quite evident how collisions affect the diffusion more in the high-pressure scenario, where the number density variation at the radial periphery increases by a factor of 10. The low-power case seems to be almost unaffected; this can be explained by looking once again at Fig. 3. The radial profiles have been chosen at the axial position of $z = 5$ mm. At this distance from the source tube exit, for low-power, the neutral gas density from the source is greater with respect to the background ($n_{g*}^{\text{plume}} \sim 10^{19}$ m^{-3}), therefore the effect of additional neutrals is negligible. The same cannot be stated for the high-power case; in fact, with the neutral density of the same magnitude as the ambient one, the additional scattering caused by interactions highly affects the plume topology.

Considering Fig. 5(b) it is clear how the radial component of ϕ presents a different behaviour. The potential drop in the high-pressure high-power case is far more accentuated, hence the ion confinement is less effective [23]. As a consequence, a more pronounced secondary expansion is present and a less-collimated plume can be observed. The tendency of the plasma beam to spread in the radial direction (i.e. the presence of a less effective magnetic confinement) can be seen also in Fig. 5(c), where the electron temperature is shown as a function of the radial position. It is quite evident that the population

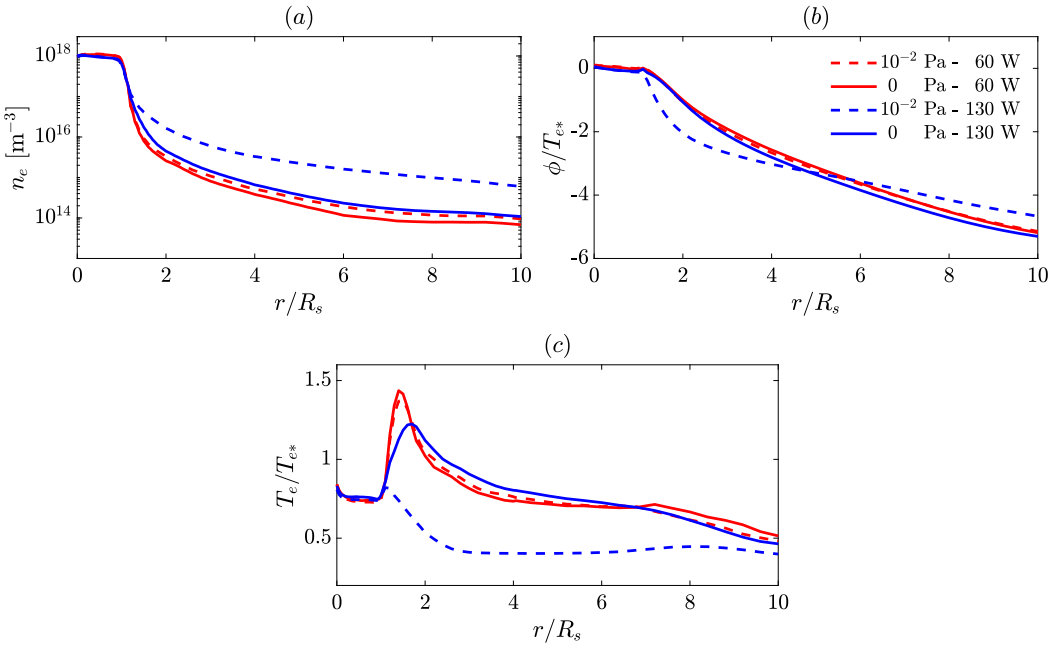

Fig. 5. Comparison between (a) radial ion number density (b) radial plasma potential (c) electron temperature at different background pressure for operating power 60 W and 130 W.

Table 3
Normalised plasma potential at infinity ϕ_∞ for increasing background pressure at different operation power P_a.

p_{back} [Pa]	ϕ_∞/T_{e*}	
	P_a = 60 W	P_a = 130 W
0	−7.0	−6.9
10^{-4}	−7.0	−6.9
10^{-3}	−7.0	−6.8
10^{-2}	−6.8	−6.3

Table 4
Normalised thrust F/F_0 and percentage variation ε for increasing background pressure at different operation power P_a.

p_{back} [Pa]	P_a = 60 W		P_a = 130 W	
	F/F$_0$	ε	F/F$_0$	ε
0	1.44	0	1.49	0
10^{-4}	1.44	−0.13	1.49	−0.09
10^{-3}	1.43	−0.33	1.47	−1.32
10^{-2}	1.42	−1.20	1.29	−13.63

of electrons that is able to escape the MN confinement is of a higher temperature. The behaviour of this high-energy escaping population is barely affected by the pressure variation when the operating power is limited (the overall electron number density is almost constant along the radius), whereas, at increasing power, the magnetic confinement is overcome also by low-energy particles, that are able to pass the OMFL due to the radial momentum component induced by collision. As a consequence, the temperature peak becomes extremely limited and the electron population quickly cools down until a plateau is reached. The values of plasma potential at infinity can be found in Table 3. It is clear the potential drop reduces in magnitude with increasing pressure, decreasing the ambipolar ion acceleration, resulting in a lower thrust. The detriment is larger for the high-power case (~10%), starting with $\phi_\infty/T_{e*} \simeq -6.9$ up to $\phi_\infty/T_{e*} \simeq -6.3$; adversely, the low-power potential drop reduction is essentially negligible (<3%).

Fig. 6 shows the axial profiles of n_e and u_i. Considering Fig. 6(a) it is fairly reasonable to state that the on-axis electron distribution is not affected by the background neutral population. The effect of the decreasing potential drop in the axial direction is quite evident when looking at Fig. 6(b), where the axial ion velocity u_i is presented normalised by the inlet Bohm speed $c_i = \sqrt{k_b T_{e*}/m_i}$. The initial decrease of the ion velocity is due to collisions (e.g. charge exchange interactions) taking place right after the particles injection in the domain. As expected, the axial variation of the low-power cases is small (<5%). Instead, the difference becomes quite considerable at 130 W (~22%), where the ion velocity begins to diverge from the general trend at $z = 20$ mm.

4.4. Propulsive performance

The analysis of the plasma profiles highlighted how a substantial difference is introduced at high-pressure. In this section, the effect of such variation on the propulsive parameters will be investigated.

The propulsive performance of the cathode-less RF thruster has been reported in Table 4. It is quite evident how the high-power case is more affected by the increase of the facility pressure, showing a decisive performance degradation of $\varepsilon = 13.63\%$ at $p_{\text{back}} = 10^{-2}$ Pa, where ε is defined as

$$\varepsilon = \frac{\| F - F_{p_{\text{back}}=0\ \text{Pa}} \|}{\| F_{p_{\text{back}}=0\ \text{Pa}} \|} \times 100. \tag{26}$$

The 60 W case presents a negligible thrust reduction until the background neutral density becomes closer to the order of the gas emitted by the source (i.e. 10^{18} m^{-3}). Even in this case, however, the thrust reduction is more limited with respect to the high-power scenario.

The trend of the normalised thrust for the four power levels is shown in Fig. 7. It is clear how the thruster performance is not affected by neutrals in the same way for all the various cases. The value of 10^{-3} Pa seems to be a threshold over which the performance drop becomes non-negligible when the thruster is operated at a relatively high-power (e.g. 130 W).

Plotting the performance loss ε as a function of the source plasma temperature T_{e*} for different pressure levels yields Fig. 8. While low neutral density cases are characterised by a limited ε throughout the temperature range, a different scenario emerges when the pressure increases. It is quite evident how the slope changes when larger values of T_e are involved. This threshold level could be identified as $T_e \sim 8$ eV

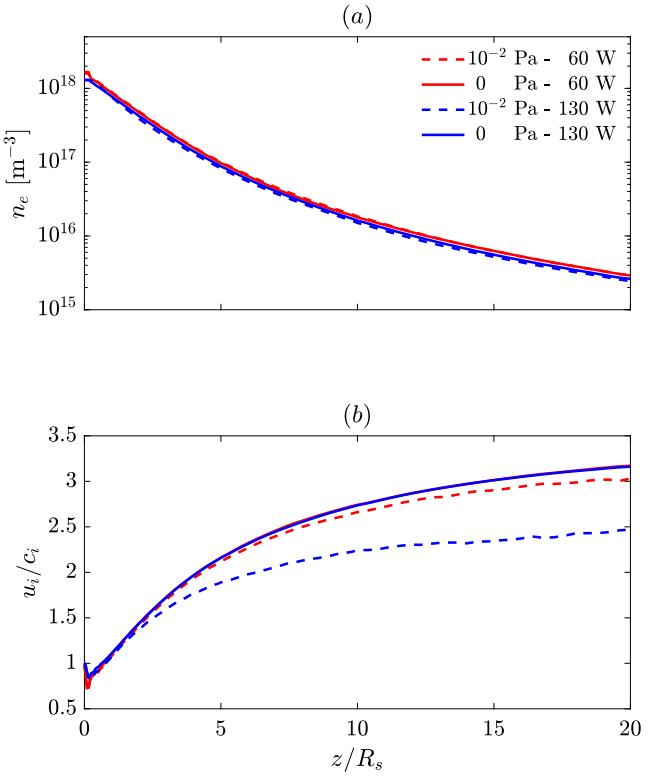

Fig. 6. Comparison between (a) axial electron number density and (b) normalised axial ion velocity at different background pressure for absorbed power 60 W (continuous line) and 130 W (dashed line).

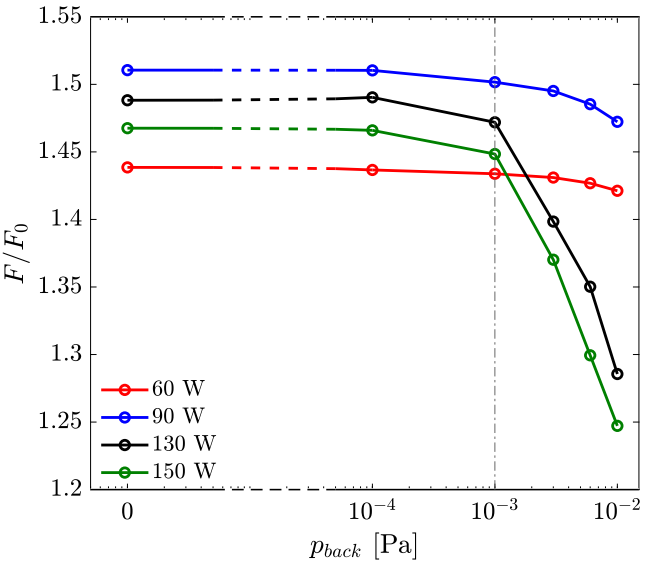

Fig. 7. Normalised thrust for increasing background pressure p_{back} at different operating powers.

(vertical dashed line in Fig. 8), where excitation and ionisation rates become non-negligible. In fact, as it will be presented in the following section, the ionisation phenomenon becomes of main relevance when considering the higher power cases (i.e. 130 W and 150 W); adversely, at 60 W and 90 W the average energy of electrons is not enough to trigger ionisation interactions. If the electron temperature exceeds the excitation/ionisation energies of the neutral species, facility effects

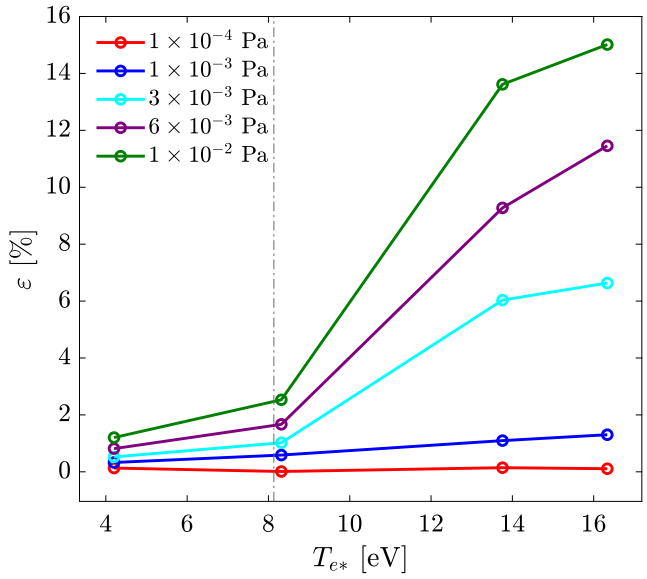

Fig. 8. Thrust loss ε for increasing plasma temperatures at different background pressure levels.

Table 5
Efficiencies for increasing background pressure at different absorbed powers P_a.

p_{back} [Pa]	P_a = 60 W			P_a = 130 W		
	η_{conv}	η_{div}	η_{MN}	η_{conv}	η_{div}	η_{MN}
0	0.71	0.63	0.57	0.72	0.62	0.55
10^{-4}	0.72	0.63	0.57	0.72	0.62	0.55
10^{-3}	0.71	0.63	0.56	0.71	0.60	0.54
10^{-2}	0.66	0.62	0.52	0.63	0.48	0.42

become non-negligible; bearing in mind that the neutral gas plume from the source tube also plays a crucial role in the sensitivity of the thruster to the cold gas background. In general, facility effects must be considered if electron energies in the plume approach levels for significant inelastic collisions.

Considering now the previously defined efficiencies, Table 5 shows how they change as the neutral density increases. In detail, the low-power case thermal conversion and overall MN efficiencies seem to only be slightly affected at the highest pressure levels, both presenting a decrease of 0.05. In contrast, the ion divergence efficiency is quite unscathed, with a reduction of 0.01. As is conceivable, increasing the background pressure at high-power levels gives rise to a harsh drop of the thruster performance parameters, namely 0.09 for η_{conv}, 0.14 for η_{div} and 0.13 for η_{MN}.

Fig. 9 shows the different normalised collisional power losses, i.e. the power that ions and electrons lose to neutrals due to elastic and inelastic interactions. The portrayed quantities have been evaluated by means of Eq. (20). The subscript refers to the particular interaction: ion–neutral charge exchange (*cex*), ion–neutral momentum exchange (*mex*), electron–neutral ionisation (*ion*), electron–neutral lumped excitation 1S and 2P (*1S* and *2P* respectively), and electron–neutral elastic scattering (*scat*). As expected, collision-related losses considerably increase while increasing the neutral number density up to 10^{18} m^{-3}. Considering first the low-power regime in Fig. 9, it is quite evident how the two main interactions losses are the ion–neutral momentum exchange (P_{mex}) and charge exchange (P_{cex}). Other collisional terms are negligible due to their low frequency. The main reason is that the average energy possessed by the electrons produced in a low-power scenario is not enough to consistently cause excitation and ionisation phenomena. Only the electron population of the high velocity tail of

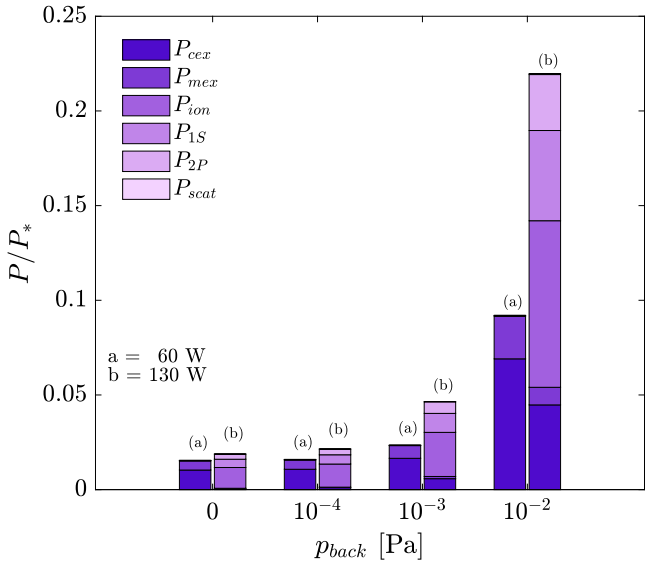

Fig. 9. Normalised power losses caused by collision for increasing background pressure p_{back} at different operating power (a) 60 W and (b) 130 W.

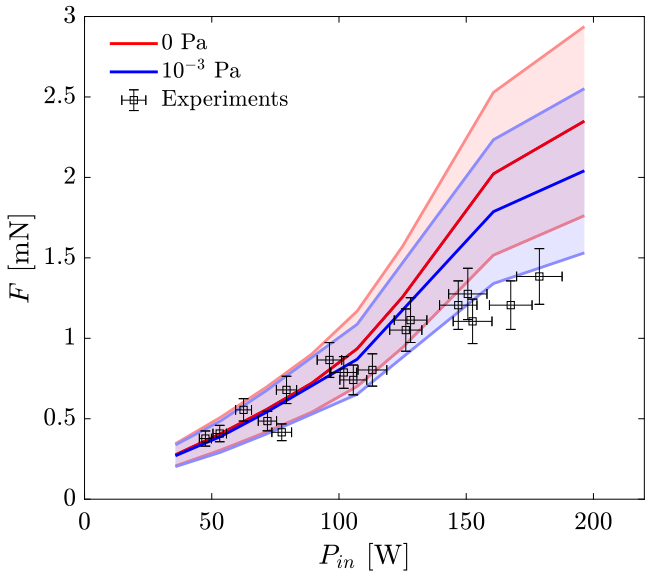

Fig. 10. Thrust evaluated for different pressure levels against experimental measures.

the distribution is able to trigger those interactions, causing the overall power contribution to be negligible.

A different scenario is presented for the 130 W case where ionisation interaction becomes the main cause of energy loss. Excitation processes are non-negligible as well. For the lower background pressure cases, charge and momentum exchange phenomena seem to be negligible, becoming of relevant importance only for $P_a > 10^{-3}$, where their power losses are quite close to the excitation ones.

Taking a more general look to the plot reveals how the presence of a background neutral gas density highly affects the total power loss caused by inter-species interactions, starting from a mere 2% of the total power delivered to the plume up to approximately 10% and 22% for the low and high-power cases respectively.

4.5. Thrust comparison and limiting assumptions

To test the validity of the findings, this section will compare the numerical results to experimental measures of thrust that have been made at finite background pressure. Measurements have been performed at the High Vacuum Facilities of the University of Padova; a vacuum chamber of radius 0.3 m and length 2 m, maintained at a working pressure of circa 10^{-3} Pa. A detailed description of the experimental setup can be found in Ref. [6]. The thrust balance is described in Ref. [53]; measurement errors are estimated to be approximately 25% for thrust and 10% for the operating power [53]. At the same time, the numerical error bands arise from different factors, such as assumptions in the GSM and uncertainty in the radio-frequency efficiency, as well as the uncertainty in collision cross sections used both in the GSM and in the PIC [28], and statistical variance in the PIC method [23]. The error bands are approximately of 25% of the simulated thrust. Fig. 10 presents the estimated thrust values from the numerical suite for 0 and 10^{-3} Pa against the experimental measures (note $P_{in} = P_a/\eta_{RF}$). For the ideal vacuum simulations, there is good agreement between $P_{in} = 50 - 120$ W; the experimental measure lie within the 25% error of the numerical model. However, at higher values of P_{in} it is clear that the numerical routine increasingly overestimates the thrust, with an error of +59% at 180 W. As already seen, the introduction of a background neutral population, that replicates the facility environment, decreases the thrust, reducing the overestimation. The plateau of experimental thrust at increasing power (and increasing T_e) might well be explained by losses in MN efficiency due to the chamber pressure. The agreement with experiments is considered acceptable (<30%) since the numerical model is affected by several assumptions. For example, the effects of background density on the ionisation process of the source region have been neglected. In a real scenario, the overall source ion-neutral ratio might change with increasing pressure, contributing to the thruster performance alteration.

The numerical acceleration methods might also introduce some additional error. However, a study conducted by Andrews et al. [23] has shown how the thrust estimation is basically unaffected (variation lower than 1%) by γ and f as long as their value remains limited to a reasonable range ($\gamma < 50$ and $f = 250$).

In the PIC, the neutral gas field is included with a uniform distribution. In practice, the position of the vacuum pumps and material sputtering would affect the local background density. It was seen in Fig. 8 that significant thrust losses can result from even small increases in pressure beyond 10^{-3} Pa, and there may be a significant uncertainty in the assumed working pressure at the MN throat region.

5. Conclusion

The main goal of this work was the investigation of facility effects on the performance of a cathode-less RF thruster MN. Several levels of background pressures have been tested for four different operational regimes: low-power 60 W and 90 W and high-power 130 W and 150 W cases were considered for the study.

The additional background neutral population caused a degradation of the thruster performance due to the decisive increase of the electron–neutral and ion–neutral elastic and inelastic interactions. For low-power (i.e. low plasma temperature), the average energy possessed by electrons was too low to generate ionisation and excitation interactions in a consistent way. As a consequence, the main factors of power loss in that case were proven to be ion-neutral charge and momentum exchange. Adversely, in the 130–150 W cases, electron-based inelastic collisions dominated the plume causing up the 70% of the total power losses.

These enhanced collision rates resulted in an overall thrust decrease, with a more decisive impact in the high-power scenario, where a drop of more than 13% was observed. The low-power case presented a decreasing trend in the performance as well. However, the thrust depletion was limited to less than 2% even at the highest background pressure level. This effect is related to the higher neutral particle count that is ejected by the source when operating the thruster at low-power,

causing the plume to have a similar or even higher neutral density than the background for the first portion of the domain.

In conclusion, facility effects definitely represent an issue in the characterisation of RF source-based MEPTs: once the plasma temperature of the plume becomes high enough (say > 8 eV for xenon) to cause ionisation collisions in a consistent manner, performing measurements for high-power level regimes at a pressure circa 10^{-3} Pa, or higher, may yield less accurate results. Despite being less affected by the ambient neutral count, low-power thrusters (i.e. characterised by $T_e < 8$ eV) should also be kept at a pressure lower than 10^{-3} Pa, in order to avoid undesired facility-related performance drop due to ion–neutral collisions.

Declaration of competing interest

The authors declare that they have no known competing financial interests or personal relationships that could have appeared to influence the work reported in this paper.

Acknowledgements

We acknowledge Technology for Propulsion and Innovation (T4i) S.p.A. for the support provided in the development of this work. We also acknowledge the CINECA, Italy award, under the ISCRA initiative, for the availability of high-performance computing resources and support.

Appendix. Global model

In this appendix, the expressions for the evaluation of Eqs. (1) and (2) have been reported. For a more detailed description of the model as a whole, the reader is referred to [54,55]. Starting with Eq. (1),

$$R^I_{chem} = \sum_J K_{JI} n_J n_e - \sum_J K_{IJ} n_I n_e \tag{A.1}$$

is the species density flux associated to chemical reactions, where K_{IJ} is the rate constant for inelastic transition from species I to J. The term

$$R^I_{wall} = \frac{S^I_{wall}}{\mathcal{V}} \Gamma^I_{wall} \tag{A.2}$$

is related to wall production and losses. Here, $\mathcal{V} = \mathcal{L}\pi\mathcal{R}^2$ represents the volume of the source ($\mathcal{R}$ and $\mathcal{L}$ being the source radius and length, respectively), $\Gamma^I_{wall} = n_I u_B$ is the particle flux, u_B being the Bohm speed. Lastly, S^I_{wall} is an equivalent source (or wall) surface; for a closed cylinder with cusps, the surface is given as

$$S^I_{wall} = 2\pi\mathcal{R}h_L\beta + h_{R\perp}(2\pi\mathcal{R}\mathcal{L} - S_{cusps} + h_{R\parallel})S_{cusps}. \tag{A.3}$$

Despite the assumption of a uniform magnetostatic field, the presence of cusps is included by means of an empirical model. The evaluation of the cusp area can hence be performed as shown by Goebel et al. [56],

$$S_{cusps} = 4N_{cusps}\sqrt{r_{ce}r_{ci}}2\pi\mathcal{R}. \tag{A.4}$$

Within these two expressions, h_L, h_R and β are semi-empirical coefficients that take into account the non-uniformity of the plasma profiles [57]. N_{cusps} is the number of magnetic cusps, while r_{ci} and r_{ce} are the ion and electron cyclotron radii, respectively.

The last term of Eq. (1) is the flux density at the source outlet,

$$R^I_{ex} = \frac{S^I_{ex}}{\mathcal{V}} \Gamma^I_{ex}, \tag{A.5}$$

where S^I_{ex} is the physical area of the exit section (A_0), $\Gamma^e = \Gamma^i = n_e u_B$ for ions and electrons while the neutral flux is computed assuming free molecular regime $\Gamma^g = 1/4 n_g u_{th}$ (u_{th} being the neutrals thermal speed).

In the case of the electron power balance of Eq. (2), the chemical contribution is taken as

$$P_{chem} = \sum_I \sum_J K_{IJ} n_I n_e \Delta U_{IJ} + \sum_I K_{II} n_I n_e \frac{3m_e}{m_I} T_e, \tag{A.6}$$

where ΔU_{IJ} represents the energy difference between species I and J in eV. Regarding the elastic collision term, K_{II} is the rate constant for the interaction between species I and electrons, while m_I refers to the species I mass. The wall/source term for the wall–plasma interaction can be evaluated as [46,58]

$$P_{wall} = R^e_{wall}\left(\frac{5}{2} + \frac{1}{2}\log\sqrt{\frac{m_i}{2\pi m_e}}\right) T_e. \tag{A.7}$$

Note that for expressions Eqs. (A.3) and (A.7) to be valid, the Bohm sheath criterion at the source wall is assumed [30]. Similarly, the exhaust power contribution P_{ex} reads

$$P_{ex} = R^e_{ex}\left(\frac{5}{2} + \frac{1}{2}\log\sqrt{\frac{m_i}{2\pi m_e}}\right) T_e. \tag{A.8}$$

The computation of the reaction rate coefficient K_{IJ} is carried out through

$$K = \sqrt{\frac{2q}{m_e}} \int_0^\infty \varepsilon\sigma f_0 d\varepsilon, \tag{A.9}$$

where q and ε are the electron charge and energy (in eV), respectively. σ is the collision cross-section for the generic particle reaction, whereas f_0 is the electron energy distribution function (EEDF). Within this study, the hypothesis of a Maxwellian distribution is made [59]:

$$f_0(\varepsilon) = 2\sqrt{\frac{1}{T_e^3\pi}} \exp\left(-\frac{\varepsilon}{T_e}\right). \tag{A.10}$$

References

[1] M. Keidar, T. Zhuang, A. Shashurin, G. Teel, D. Chiu, J. Lukas, S. Haque, L. Brieda, Electric propulsion for small satellites, Plasma Phys. Control. Fusion 57 (1) (2014) 014005, http://dx.doi.org/10.1088/0741-3335/57/1/014005.
[2] M. Manente, F. Trezzolani, M. Magarotto, E. Fantino, A. Selmo, N. Bellomo, E. Toson, D. Pavarin, Regulus: A propulsion platform to boost small satellite missions, Acta Astronaut. 157 (2019) 241–249.
[3] H. Kuninaka, S. Satori, Development and demonstration of a cathodeless electron cyclotron resonance ion thruster, J. Propuls. Power 14 (1998) 1022–1026.
[4] M. Magarotto, M. Manente, F. Trezzolani, D. Pavarin, Numerical model of a helicon plasma thruster, IEEE Trans. Plasma Sci. 48 (4) (2020) 835–844.
[5] N. Souhair, et al., Simulation and modelling of an iodine fed helicon plasma thruster, in: 37^{Th} International Electric Propulsion Conference, Cambridge, USA, 2022, no. IEPC-2022-496.
[6] N. Bellomo, M. Magarotto, M. Manente, et al., Design and in-orbit demonstration of regulus, an iodine electric propulsion system, CEAS Space J. 14 (2022) 79–90.
[7] Y. Nakagawa, K. Koizumi, Y. Naito, K. Komurasaki, Water and xenon ECR ion thruster—comparison in global model and experiment, Plasma Sources. Sci. Technol. 29 (2020) 105003.
[8] T. Andreussi, E. Ferrato, C. Paissoni, A. Kitaeva, V. Giannetti, A. Piragino, S. Schäff, K. Katsonis, C. Berenguer, Z. Kovacova, E. Neubauer, M. Tisaev, B. Karadag, A. Fabris, M. Smirnova, A. Mingo, D. Quang, Z. Alsalihi, F. Bariselli, T. Magin, The AETHER project: development of air-breathing electric propulsion for VLEO missions, CEAS Space J. 14 (2022) 717–740, http://dx.doi.org/10.1007/s12567-022-00442-3.
[9] S. Mazouffre, Electric propulsion for satellites and spacecraft: established technologies and novel approaches, Plasma Sources. Sci. Technol. 25 (2016) 033002.
[10] J. Jarrige, P.-Q. Elias, D. Packan, Measurement of ion acceleration in the magnetic nozzle of an ECR plasma thruster, in: Space Propulsion 2014, Cologne, Germany, 2014, no. 2980896.
[11] Z. Zhang, Z. Zhang, S. Xu, W.Y.L. Ling, J. Ren, H. Tang, Three-dimensional measurement of a stationary plasma plume with a faraday probe array, Aerosp. Sci. Technol. 110 (2021) 106480.
[12] E. Dale, B. Jorns, A. Gallimore, Future directions for electric propulsion research, Aerospace 7 (2020) 120, http://dx.doi.org/10.3390/aerospace7090120.
[13] C. Cai, Numerical studies on plasma plume flows from a cluster of electric propulsion devices, Aerosp. Sci. Technol. 41 (2015) 134–143.
[14] D. Packan, et al., The "minotor" H2020 project for ECR thruster development, in: 35^{Th} International Electric Propulsion Conference, Atlanta, USA, 2017, no. IEPC-2017-547.

[15] T. Vialis, J. Jarrige, D.M. Packan, Geometry optimization and effect of gas propellant in an electron cyclotron resonance plasma thruster, in: International Electric Propulsion Conference, Atlanta, Georgia, 2017, no. IEPC-2017-378.

[16] N. Caruso, M. Walker, Neutral ingestion effects on plume properties of a radio-frequency plasma discharge, J. Propuls. Power 34 (2018) 58–65.

[17] A. Piragino, F. Faraji, M. Reza, E. Ferrato, A. Piraino, T. Andreussi, Background pressure effects on the performance of a 20 kw magnetically shielded hall thruster operating in various configurations, Aerospace 8 (2021) 69.

[18] R.F. Thomas Kerber, M. Baird, K. Lemmer, Background pressure effects on plume properties of a low-cost hall effect thruster, in: 36th International Electric Propulsion Conference, Vienna, Austria, 2019.

[19] A. Piragino, F. Faraji, M. Reza, E. Ferrato, A. Piraino, T. Andreussi, Background pressure effects on the performance of a 20 kw magnetically shielded hall thruster operating in various configurations, Aerospace 8 (3) (2021).

[20] W. Hargus, L. Tango, M. Nakles, Background pressure effects on krypton hall effect thruster internal acceleration, in: 33rd International Electric Propulsion Conference, Washington, DC, 2013.

[21] J.S. Snyder, G. Lenguito, J.D. Frieman, T.W. Haag, J.A. Mackey, Effects of background pressure on SPT-140 hall thruster performance, J. Propuls. Power 36 (5) (2020) 668–676.

[22] T. Collard, J. B., Magnetic nozzle efficiency in a low power inductive plasma source, Plasma Sources. Sci. Technol. 28 (2019) 105019.

[23] S. Andrews, S.D. Fede, M. Magarotto, Fully kinetic model of plasma expansion in a magnetic nozzle, Plasma Sources. Sci. Technol. 31 (3) (2022) 035022, http://dx.doi.org/10.1088/1361-6595/ac56ec.

[24] B. Wachs, B. Jorns, Effect of background pressure on ion dynamics in an electron cyclotron resonance thruster, in: 2018 Joint Propulsion Conference, Cincinnati, USA, 2018, no. AIAA 2018-4585.

[25] B. Wachs, B. Jorns, Background pressure effects on ion dynamics in a low-power magnetic nozzle thruster, Plasma Sources. Sci. Technol. 29 (2020) 045002, http://dx.doi.org/10.1088/1361-6595/ab74b6.

[26] M. Magarotto, S. Di Fede, N. Souhair, S. Andrews, F. Ponti, Numerical suite for cathodeless plasma thrusters, Acta Astronaut. 197 (2022) 126–138, http://dx.doi.org/10.1016/j.actaastro.2022.05.018.

[27] S. Andrews, R. Andriulli, N. Souhair, S. Di Fede, D. Pavarin, F. Ponti, M. Magarotto, Coupled global and PIC modelling of the regulus cathode-less plasma thrusters operating on xenon, iodine and krypton, Acta Astronaut. 207 (2023) 227–239, http://dx.doi.org/10.1016/j.actaastro.2023.03.015.

[28] N. Souhair, M. Magarotto, E. Majorana, F. Ponti, D. Pavarin, Development of a lumping methodology for the analysis of the excited states in plasma discharges operated with argon, neon, krypton, and xenon, Phys. Plasmas 28 (2021) 093504, http://dx.doi.org/10.1063/5.0057494.

[29] E. Majorana, N. Souhair, F. Ponti, M. Magarotto, Development of a plasma chemistry model for helicon plasma thruster analysis, Aerotech. Missili Spazio 100 (2021) 225–238, http://dx.doi.org/10.1007/s42496-021-00095-1.

[30] M. Guaita, M. Magarotto, M. Manente, D. Pavarin, M. Lavagna, Semi-analytical model of a helicon plasma thruster, IEEE Trans. Plasma Sci. 50 (2022) 425–438, http://dx.doi.org/10.1109/TPS.2022.3146088.

[31] F. Marmuse, Iodine plasmas : experimental and numerical studies. Application to electric propulsion (Ph.D. thesis), Sorbonne Université, 2020, no. 2020SORUS110.

[32] L. Brieda, M. Keidar, Development of the starfish plasma simulation code and update on multiscale modeling of hall thrusters, in: 48^{Th} AIAA/ASME/SAE/ASEE Joint Propulsion Conference & Exhibit, Atlanta, GA, USA, 2012, no. AIAA 2012-4015.

[33] S. Di Fede, M. Magarotto, S. Andrews, D. Pavarin, Simulation of the plume of a magnetically enhanced plasma thruster with SPIS, J. Plasma Phys. 87 (2021) 905870611, http://dx.doi.org/10.1017/S0022377821001057.

[34] P. Jiménez, M. Merino, E. Ahedo, Wave propagation and absorption in a helicon plasma thruster and its plume, Plasma Sources. Sci. Technol. 31 (4) (2022) 045009, http://dx.doi.org/10.1088/1361-6595/ac5ecd.

[35] F.F. Chen, D.D. Blackwell, Upper limit to Landau damping in helicon discharges, Phys. Rev. Lett. 82 (1999) 2677–2680.

[36] M. Magarotto, S. Di Fede, N. Souhair, S. Andrews, F. Ponti, Numerical suite for cathodeless plasma thrusters, Acta Astronaut. 197 (2022) 126–138.

[37] G. Gallina, M. Magarotto, M. Manente, D. Pavarin, Enhanced bidimensional pic: an electrostatic/magnetostatic particle-in-cell code for plasma based systems, J. Plasma Phys. 85 (2019) 905850205, http://dx.doi.org/10.1017/S0022377819000205.

[38] G. Bird, The DSMC Method, CreateSpace Independent Publishing Platform, 2013.

[39] A. Guthrie, K. Wakerling, R., The Characteristics of Electrical Discharges in Magnetic Fields, first ed., McGraw-Hill New York, 1949.

[40] Plasma, Plasma diagnostic techniques / edited by Richard H. Huddlestone and Stanley L. Leonard, in: Plasma Diagnostic Techniques, in: Pure and applied physics 21, Academic Press, New York, 1965.

[41] Y. Weng, M.J. Kushner, Method for including electron-electron collisions in Monte Carlo simulations of electron swarms in partially ionized gases, Phys. Rev. A 42 (1990) 6192–6200, http://dx.doi.org/10.1103/PhysRevA.42.6192.

[42] J. Szabo, Fully kinetic numerical modeling of a plasma thruster (Ph.D. thesis), Massachusetts Institute of Technology, 2001.

[43] Y.V. Esipchuk, G.N. Tilinin, Drift instability in a hall-current plasma accelerator, Sov. Phys. - Tech. Phys. (Engl. Transl.); (U. S.) 21:4 (1976).

[44] J. Szabo, N. Warner, M. Martinez-Sanchez, O. Batishchev, Full particle-in-cell simulation methodology for axisymmetric hall effect thrusters, J. Propuls. Power 30 (2014) 197–208, http://dx.doi.org/10.2514/1.B34774.

[45] F.F. Chen, Introduction To Plasma Physics and Controlled Fusion, vol. 1, Springer, 1984.

[46] E. Ahedo, J. Navarro-Cavallé, Helicon thruster plasma modeling: Two-dimensional fluid-dynamics and propulsive performances, Phys. Plasmas 20 (2013) 043512, http://dx.doi.org/10.1063/1.4798409.

[47] J.A. Bittencourt, Fundamentals of Plasma Physics, Springer Science & Business Media, 2004.

[48] K. Emoto, K. Takahashi, Y. Takao, Vector resolved energy fluxes and collisional energy losses in magnetic nozzle radiofrequency plasma thrusters, Front. Phys. 9 (2021).

[49] S.J. Araki, R.E. Wirz, Ion–neutral collision modeling using classical scattering with spin-orbit free interaction potential, IEEE Trans. Plasma Sci. 41 (3) (2013) 470–480, http://dx.doi.org/10.1109/TPS.2013.2241457.

[50] I.D. Boyd, C. Cai, M.L.R. Walker, A.D. Gallimore, Computation of neutral gas flow from a hall thruster into a vacuum chamber, AIP Conf. Proc. 663 (1) (2003) 541–548.

[51] C. Cai, I.D. Boyd, Q. Sun, Rarefied background flow in a vacuum chamber equipped with one-sided pumps, J. Thermophys. Heat Transfer 20 (3) (2006) 524–535.

[52] A. Passaro, A. Vicini, L. Biagioni, Plasma thruster plume simulation: Effect of vacuum chamber environment, in: 35th AIAA Plasmadynamics and Lasers Conference, 2004.

[53] F. Trezzolani, M. Magarotto, M. Manente, D. Pavarin, Development of a counter-balanced pendulum thrust stand for electric propulsion, Measurement 122 (2018) 494–501, http://dx.doi.org/10.1016/j.measurement.2018.02.011.

[54] F.J. Bosi, Global model of microwave plasma assisted N2O dissociation for monopropellant propulsion, Phys. Plasmas 26 (3) (2019) 033510.

[55] J.L. M. Lieberman, Principles of Plasma Discharges and Materials Processing, John Wiley and Sons, 2005.

[56] M. Goebel, I. Katz, Fundamentals of Electric Propulsion: Ion and Hall Thrusters., John Wiley & Sons, 2008.

[57] C. Lee, M.A. Lieberman, Global model of Ar, O2, Cl2, and Ar/O2 high-density plasma discharges, J. Vacuum Sci. Technol. A 13 (2) (1995) 368–380.

[58] T. Lafleur, Helicon plasma thruster discharge model, Phys. Plasmas 21 (4) (2014) 043507, http://dx.doi.org/10.1063/1.4871727.

[59] G.J.M. Hagelaar, L.C. Pitchford, Solving the Boltzmann equation to obtain electron transport coefficients and rate coefficients for fluid models, Plasma Sources. Sci. Technol. 14 (4) (2005) 722.